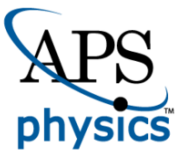

Anisotropically large anomalous and topological Hall effect in a kagome magnet

Gyanendra Dhakal, Fairoja Cheenicode Kabeer, Arjun K. Pathak, Firoza Kabir, Narayan Poudel, Randall Filippone, Jacob Casey, Anup Pradhan Sakhya, Sabin Regmi, Christopher Sims, Klauss Dimitri, Pietro Manfrinetti, Krzysztof Gofryk, Peter M. Oppeneer, and Madhab Neupane

Phys. Rev. B **104**, L161115 — Published 26 October 2021

DOI: 10.1103/PhysRevB.104.L161115

Anisotropically large anomalous and topological Hall effect in a kagome magnet

Gyanendra Dhakal,[1,*] Fairoja Cheenicode Kabeer,[2,*] Arjun K. Pathak,[3,*] Firoza Kabir,[1,*] Narayan Poudel,[4] Randall Filippone,[3] Jacob Casey,[3] Anup Pradhan Sakhya,[1] Sabin Regmi,[1] Christopher Sims,[1] Klauss Dimitri,[1] Pietro Manfrinetti,[5,6] Krzysztof Gofryk,[4] Peter M. Oppeneer,[2] and Madhab Neupane[1,†]

[1] *Department of Physics, University of Central Florida, Orlando, Florida 32816, USA*
[2] *Department of Physics and Astronomy, Uppsala University, P. O. Box 516, S-75120 Uppsala, Sweden*
[3] *Department of Physics, SUNY Buffalo State, Buffalo, New York 14222, USA*
[4] *Idaho National Laboratory, Idaho Falls, ID 83402, USA*
[5] *Department of Chemistry, University of Genova, 16146 Genova, Italy*
[6] *Institute SPIN-CNR, 16152 Genova, Italy*

(Dated: October 12, 2021)

Recently, kagome materials have become an engrossing platform to study the interplay among symmetry, magnetism, topology, and electron correlation. The latest works on RMn$_6$Sn$_6$ (R = rare earth metal) compounds have illustrated that this family could be intriguing to investigate various physical phenomena due to large spin-orbit coupling and strong magnetic ordering. However, combined transport and spectroscopic studies in RMn$_6$Sn$_6$ materials are still limited. Here, we report magnetic, magneto-transport, and angle-resolved photoemission spectroscopy measurements of a kagome magnet ErMn$_6$Sn$_6$ that undergoes antiferromagnetic (T_N = 345 K) to ferrimagnetic (T_C = 68 K) phase transitions in the presence of field. We observe large anomalous and topological Hall effects serving as transport signatures of the nontrivial Berry curvature. The isothermal magnetization exhibits strong anisotropic nature and the topological Hall effect of the compound depends on the critical field of metamagnetic transition. Our spectroscopic results complemented by theoretical calculations show the multi-orbital kagome fermiology. This work provides new insight into the tunability and interplay of topology and magnetism in a kagome magnet.

The interplay among magnetism, correlation, and topology has captured enormous attention currently owing to exotic transport and electronic behaviors [1–5]. The kagome lattice, a two-dimensional network of a triangular Bravais lattice sharing the corners, provides an opportunity to study diverse quantum magnetic phases [2, 6–10]. Due to the unusual lattice geometry and breaking of time-reversal symmetry, kagome magnets can support Dirac fermions [6, 11], intrinsic Chern quantum phases [12, 13], and spin liquid phases [14] leading to a sudden surge of research interest in these materials. Kagome lattices possessing 3d transition metals such as Fe_3Sn_2 and $Co_3Sn_2S_2$ have bolstered the research interests as they exhibit large Berry curvature fields and giant magnetization driven electron nematicity [7, 15–22]. Kagome systems with spin-orbit coupling (SOC) and out-of-plane ferromagnetic order fulfill conditions for Chern gapped Dirac fermion, that can give rise to quantum anomalous Hall effect [12, 13]. It is worth noting that binary kagome systems containing transition metals usually lack strong out-of-plane magnetization, therefore recent works are focused on the materials with strong SOC and out-of-plane magnetization which can provide an epitome of kagome materials in which one can pursue the topologically gapped Dirac fermion [9, 13, 23, 24]. One such family is rare earth (R) based RMn$_6$Sn$_6$ kagome magnet, where presence of SOC and strong magnetic order serve as an intriguing quantum key to realize near-ideal quantum limit Chern magnet [9, 24].

These rare earth 166 compounds usually reveal magnetic ordering at room temperature, with antiferromagnetic (AFM) ordering for non-magnetic R ions and ferrimagnetic (FIM) ordering for 4f- local-moment-carrying R ions [25, 26]. The compounds with R = Gd-Ho are ferrimagnetic below the Curie temperature, whereas the ones with R= Sc, Y, Tm and Lu exhibit antiferromagnetic or helimagnetic behaviors. The magnetic structure of RMn$_6$Sn$_6$ compounds consists of two different subsystems: the R and Mn subsystems. The interlayer Mn moments through the Mn-Sn1-Sn2-Sn1-Mn planes along the c-axis are always ferromagnetic whereas Mn-R-Mn and Mn-Sn-Mn magnetic moments interactions depend on the nature of the rare earth elements [27]. Interestingly, these compounds show Shubnikov-de Haas quantum oscillations below 14 T field identifying themselves as distinct type of kagome magnets [24]. Despite a few works in transport measurements [9, 12, 24, 28–30] comprehensive magnetic, transport and spectroscopic measurements of the electronic structures of these materials are still limited, therefore, understanding of the potentially interesting obscured quantum phenomena are in demand. Among these materials, ErMn$_6$Sn$_6$ shows a complex magnetic behaviour displaying several transitions. At low temperature (T<65 K) and under low or zero magnetic field, it exhibits AFM (namely AFM1) ordering due to antiparallel alignment of ferromagnetic sublattices of Er and Mn, yet even low field can change AFM to FIM state. In the intermediate temperature range 65 K$\leq$ T $\leq$ 350 K, it contains an AFM Mn sublattice and a paramagnetic (PM) Er sublattice resulting AFM state (namely AFM2) which changes to FIM under the

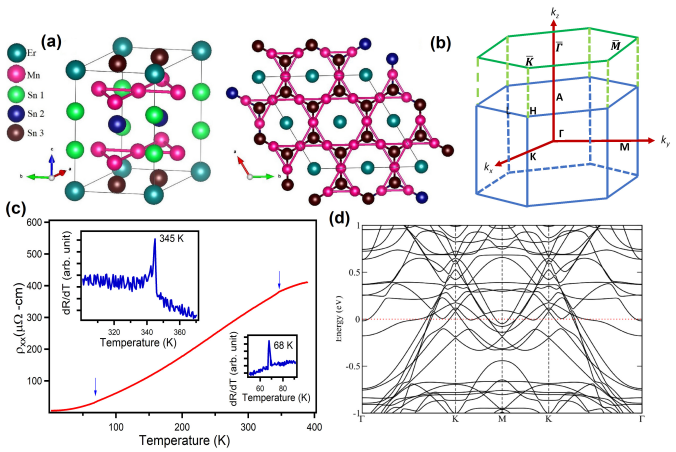

FIG. 1. Crystal structure and sample characterization of $ErMn_6Sn_6$. (**a**) Crystal structure of $ErMn_6Sn_6$. Right panel shows the top view of crystal structure forming the kagome lattice. (**b**) Bulk 3D Brillouin zone (blue) along with the projected [001] surface Brillouin zone (green), where high symmetry points are labeled. (**c**) Electrical resistivity measured as a function of temperature in zero field. The insets on the top left corner and the bottom right corner show the magnetic transitions. (**d**) First-principles calculations of the bulk band of $ErMn_6Sn_6$ with considering spin-orbit coupling (SOC).

influence of strong field. Beyond, 350 K it shows PM due to PM sublattices of Er and Mn [25, 26, 31, 32]. Therefore, $ErMn_6Sn_6$ could provide a unique system to study the evolution of transport and electronic structures with magnetic regimes.

In this article, we report magnetic, magneto-transport, and electronic structure measurements of $ErMn_6Sn_6$ in two magnetic regimes. Transport measurements show anisotropically large anomalous Hall effect (AHE) and topological Hall effect (THE) as an indication of non-trivial topology linked with the kagome material. Our angle-resolved photoemission spectroscopic (ARPES) measurements supported by first-principles calculations demonstrate the presence of multi-orbital kagome bands in the vicinity of the Fermi level with the occurrence of a Dirac-like dispersion at the K point. Our results provide a novel platform to investigate the conundrum of interplay between magnetism and topology in kagome materials.

High-quality single crystals of $ErMn_6Sn_6$ were synthesized using the Flux method (see Supplemental Material [33]). Resistivity and Hall measurements were performed in a Physical Property Measurement System (PPMS) following the conventional 4-probe method. ARPES measurements were performed at the 5-2 endstation in Stanford Synchrotron Radiation Lightsource (SSRL) beamline using a DA30L analyser. The first-principles electronic structure calculations are carried out within the density-functional theory (DFT) formalism [34–37] as implemented in the Vienna *ab initio* simulation package (VASP) [36, 37]. For details, see Sec. 1.4 of the SM [33] and Refs.[34–44] therein for details).

$ErMn_6Sn_6$ crystallizes in the hexagonal $MgFe_6Ge_6$-type structure with space group P6/mmm (No. 191) as shown in Fig. 1(a) with Er at 1(a) (0, 0, 0), Mn at 6(i) (1/2, 0, z∼0.249), Sn at 2(c) (1/3, 2/3, 0), 2(d) (1/3, 2/3, 1/2) and 2(e) (0, 0, z∼0.34) [26]. The Er and Sn3 atoms lie in the same plane and Mn-Sn1-Sn2-Sn1-Mn atoms are stacked along the c-axis alternatingly. The Mn atoms form two kagome layers and the Sn2 and Sn3 atoms form a hexagonal structure. The hexagonal structure formed by Sn3 atoms can be clearly seen from the right panel of Fig. 1(a) when viewed from the c-axis. Since Sn2 is below the Sn3 layers, it cannot be seen from this top view. The Er atoms lie at the centre of the hexagons formed by the Sn3 atoms. The Sn1 atoms lie at the centre of the hexagons of the Mn layers but they are below or above those Mn layers. The magnetic configuration is characterized by the ferromagnetic (001) Mn planes [31]. The Mn planes and the in-plane nearest neighbor Mn-Mn bonds d_{Mn-Mn}= 2.75 $\AA$ are crystallographically equivalent but the interplanar Mn-Mn bonds along the c-axis are different d_{Mn-Mn}= 4.5 $\AA$. The complex magnetic phase transitions in $ErMn_6Sn_6$ originate from the complicated interplay among the *R*-Mn, *R*-*R* and Mn-Mn exchange interactions and the competing magnetocrystalline anisotropies of the two sublattices [27]. In the antiferromagnetic state, metamagnetic behavior was also observed [26] and neutron diffraction studies have confirmed a high-temperature helimagnetic structure and a low-temperature ferrimagnetic structure in this compound [26]. In Fig. 1(b) the three-dimensional Brillouin zone is presented, which is projected onto the (001) plane forming a hexagonal pattern. Resistivity as a function of temperature, shown in Fig. 1(c), indicates the metallic nature of the sample over the measured temperature range of 2 K - 400 K. The derivative of the resistance shows two distinct peaks: the inset on the bottom right corner represents the magnetic phase transition (T_C = 68 K), and the inset on the top left corner represents another magnetic phase transition (T_N= 345 K). The first-principles calculation with SOC at the FIM phase is presented in Fig. 1(d), which shows that multiple bands cross the Fermi level indicating $ErMn_6Sn_6$ to be a metal which is in accord with the transport measurements. Electron-like bulk bands are seen along the Γ-K direction. Two Dirac dispersions are seen at the K point, one Dirac cone appears above the Fermi level, whereas another Dirac cone lies below the Fermi level. A flat band is seen ∼400 meV above the Fermi level. The bulk-band calculations in the AFM-state show some changes in the electronic structures, such as shifting of flat bands upwards (see SM for bulk-band calculations [33]). Magnetic properties as functions of both temperature and

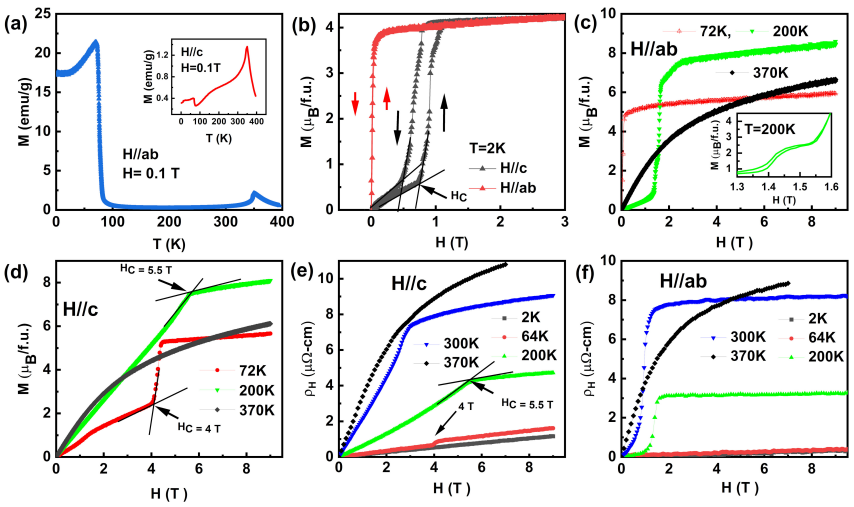

FIG. 2. Magnetic properties of $ErMn_6Sn_6$ single crystals measured along both $H//ab$ and H//c planes. (a) Magnetization as a function of temperature, M(T), measured along $H//ab$ at H = 0.1 T. Inset in (a) shows M(T) measured along $H//c$ plane at H = 0.1 T. (b) Magnetization as a function of magnetic field, M(H) measured along both $H//ab$, and $H//c$ plane at T = 2K. The M(H) was measured up to 9 T, only up to 3 T is shown for clarity. (c) and (d) Magnetization as a function of magnetic field measured along $H//ab$, and $H//c$, respectively at different temperatures. Inset in (c) shows selected part of M(H) to show the metamagnetic transition around 1.4 T at T = 200 K. Hall resistivity of $ErMn_6Sn_6$ at different temperatures with (e) $H//c$, and (f) $H//ab$ direction.

magnetic field for $ErMn_6Sn_6$ were studied along $H//ab$ and $H//c$ planes by physical property measurement system (PPMS, Quantum Design) between temperatures 2 to 400 K and magnetic field up to 9 T. The iso-field magnetization, M(T), measured along $H//ab$ at H = 0.1 T is shown in Fig. 2(a). The compound orders antiferromagnetically at $T_N = 345$ K and the magnetization is almost zero between temperatures 300 and 100 K, suggesting the AFM state. The isothermal magnetization curves, M(H), at a low magnetic field further support the AFM state in this temperature region (see Fig. 2(c)). Upon further cooling, the exchange interaction between Er and Mn sublattices becomes strong resulting in the ferrimagnetic (FIM) behavior with $T_C = 68$ K at H = 0.1 T for $H//ab$. The isothermal magnetization curves, M(H), at intermediate temperatures at a low magnetic field, further support the AFM state (see Fig. 2(c)). The application of the magnetic field shows a strong effect on the magnetic structure along the $H//c$. The M(T) measured along $H//c$ shows a similar transition in $H//ab$, however, the nature of the magnetization curves are quite different and highly anisotropic (inset, Fig. 2(a)). The value of magnetization is negligible compared to that for in $H//ab$. Comparing the M(H) for both $H//ab$ and $H//c$ (Fig. 2c, 2d), the transitions require a larger applied field for H//c. At T = 2K and $H//ab$, magnetization initially increases almost linearly with field until H$\leq$0.7 T then a sharp increase in magnetization occurs at a critical magnetic field H_c ~0.7 T, indicating the field-induced metamagnetic transition (see Fig. 2(b)). A strong change in magnetization occurs both in magnetizing and demagnetizing field with a relatively large magnetic hysteresis of 0.63 T, suggesting a field-induced first-order transition. The metamagnetic transition indicates the field-induced transformation from AFM to FIM state in $ErMn_6Sn_6$. Unlike along $H//c$, the M(H) measured along the $H//ab$, however, does not show a metamagnetic transition at the corresponding temperature, suggesting easy magnetization direction along the ab-plane. As reported by Clatterbuck and Gschneidner [25] the application of a magnetic field increases the low-temperature transition while decreasing the high-temperature transition, and the two transitions merge at H ~ 1.75 T.

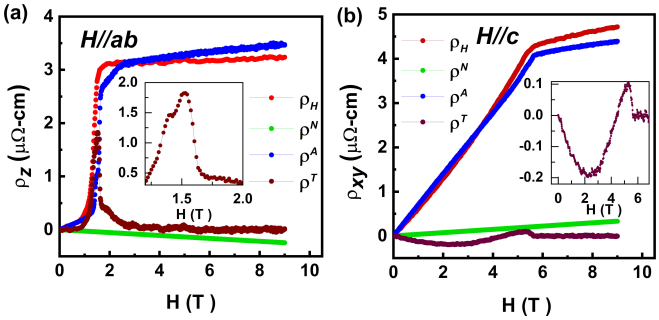

FIG. 3. Realization of anomalous and topological Hall effect. Hall resistivity and its three different components in (a) $H//ab$-plane, and (b) in $H//c$-axis at a temperature of 200 K. Inset in (a) and (b) shows ρ^T vs H for clarity along $H//ab$, and $H//c$, respectively

The saturation magnetic moments (M_s), obtained by M vs. H^{-1} graphs by extrapolating the curves to $H^{-1} = 0$ are 4.7 μ_B/f.u. and 4.3 μ_B/f.u. along $H//ab$ and $H//c$, respectively, which shows the FIM structure at high field. The critical magnetic field to induce the AFM to FIM state for $H//c$ increases until T = 170 K and slowly and decreases with further increase in temperature (e.g. Hc ~5.5 T for T = 200 K). At T = 200 K and H = 9 T, the magnetic moment is 8.47 and 8.06 μ_B/f.u. along the $H//ab$ and $H//c$, respectively which is twice the value of Ms obtained at T = 2 K.

In order to investigate the signature of the anomalous quantum Hall effect, we present the transverse resistivity response as a function of the magnetic field applied parallel to the c-axis and ab-plane as depicted in Figs. 2(e) and 2(f), respectively. The Hall resistivity follows

different trends in the different magnetic regimes. In the ferrimagnetic regime, the ρ_H does not significantly change with the field, where a small, linear increase of ρ_H is observed that does not saturate in fields up to 9 T for both $H//ab$ plane and $H//c$-axis configurations. On the other hand, in the antiferromagnetic regime, T = 200 K and 300 K, ρ_H increases rapidly with the field H$//c$ higher than the respective critical field for metamagnetic transition (Figs. 2e-2f). The overall behavior of Hall resistivity resembles the M(H) data shown in Fig. 2(c) and Fig. 2(d), respectively. Furthermore, similarly to M(H) behavior, a narrow hysteresis of ρ_H was observed in the AFM phase when the field is applied along with ab plane while no hysteretic behavior is observed for the field applied parallel to the c-axis (see Fig. S3 in SM [33] for more detail).

In topological magnetic materials, the total Hall resistivity (ρ_H) can be expressed as

$$\rho_H = \rho^N + \rho^A + \rho^T, \quad (1)$$

where, $\rho^N(H) = R_0 H$ is the normal Hall resistivity, and R_0 is dubbed as the coefficient of normal Hall resistivity, which is defined by the number of carriers (for a multiband metal system it is defined as the weighted average of the carriers with their mobilities)[28]). Similarly, $\rho^A(M) = R_S 4\pi M$ is the anomalous Hall resistivity, and ρ^T refers to the topological Hall resistivity, which originates from the Berry phase gained by electrons owing to spatially varying magnetization [45, 46]. Figure 3(a) shows the three different components of Hall resistivity at 200 K when $H//ab$. In the high field saturation region, Eq. 1 can be written as $\rho_H = R_0 H + R_S 4\pi M$. The slope R_0 and intercept $4\pi R_S$ can be estimated from the linear plot of ρ_H/M versus B/M in the high-field region. The perfect linear behavior of the ρ_H/M versus B/M at high field indicates that the anomalous Hall resistivity (ρ^A) is the dominant component in the Hall resistivity. The R_0 derived for $H//ab$ is negative whereas it is positive for $H//c$ at 200 K which gives ρ^N negative and positive, respectively as shown in Fig. 3(b). The sign change of R_0 could be the result of change in electronic structure as suggested in recent work [29, 47], it requires further investigations. The slopes $4\pi R_S$ are found to be positive for both configurations. The topological Hall resistivity (ρ^T) is estimated by subtracting normal and anomalous components of the Hall resistivity from the total Hall resistivity and its contribution is small compared to anomalous Hall resistivity in both in-plane and c-axis configuration. The topological Hall effect is more pronounced when the magnetic field is applied in the ab-plane and it reaches to 1.8 $\mu\Omega$-cm at 1.5T (Fig. 3a, inset). The obtained value of ρ^T along ab-plane in $ErMn_6Sn_6$ is 100% higher and more importantly it observed at a much lower applied magnetic field compared to YMn_6Sn_6 compound reported in ref. [28]

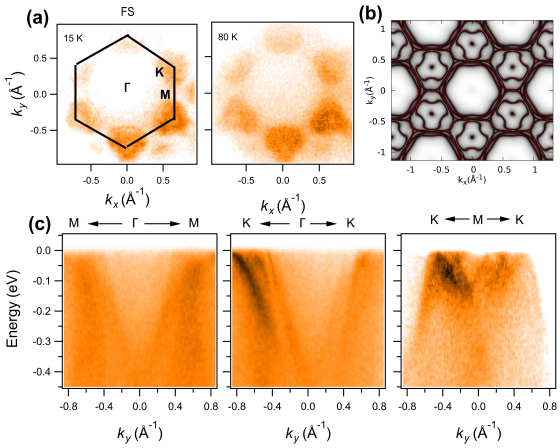

FIG. 4. Electronic structure of $ErMn_6Sn_6$. (**a**) Fermi surface map at different temperatures. The temperature values are noted in the plots. (**b**) Calculated Fermi surface map. (**c**) Dispersion maps along the M-Γ-M, K-Γ-K, and K-M-K direction, respectively the FIM phase. ARPES measurements were performed at the SSRL beamline 5-2 using 100 eV photon energy with s-polarization.

(0.75 $\mu\Omega$-cm at H=4 T and T=200 K). It is also much larger than reported for thin films correlated oxides [48] and non-cubic AFM Mn_5Si_3 [49]. Interestingly, a large anisotropic topological Hall effect of a similar magnitude to $ErMn_6Sn_6$ has been reported recently for the hexagonal non-collinear magnet, Fe_5Sn_3 [50]. In addition, ρ^T along c-plane exhibit significantly low value, but interestingly, it oscillates between negative 0.2 $\mu\Omega$-cm at 2.2 T to positive and +0.1 $\mu\Omega$-cm at 5 T (Fig. 3(b), inset). The critical magnetic field for peak in the ρ^T vs H matches excellently with that obtained from M(H) at 200 K (see Fig. 2(c) inset and Fig. 2(d)). The peak value of topological Hall resisitivity could be an indication of the presence of a new magnetic phase that may exhibit strong Hall resistivity. Further experimental and theoretical works are required to shed light on this intriguing result. Furthermore, the large difference of critical field between the ab and c-plane suggest the $ErMn_6Sn_6$ is highly anisotropy and which also play a crucial role in anomalous and topological Hall effect. The ρ^T disappears in high field region (above saturation field) indicating that it cannot host a non-trivial spin structure. Interestingly, the signs of ρ^T are opposite for the $H//ab$ and $H//c$ directions. The opposite signs of the topological Hall effect in different directions of the $ErMn_6Sn_6$ may be related to the anisotropic magnetic behavior in this material, which can induce opposite spin chirality along with the two directions [50].

In order to investigate the electronic structures of $ErMn_6Sn_6$, we performed ARPES measurements using VUV-photon source. Figure 4(a) shows Fermi surface

map parallel to the kagome plane, measured at a temperature of 15 K of 80 K, respectively. The Fermi map shows the hexagonal symmetry as suggested by the crystal structure; the circular blobs are seen at the K points, manifesting an excellent hexagonal symmetry. The intense blobs probably appear as a consequence of manifold bulk bands. Several energy pockets at the edges of the hexagonal system indicate the complex band structure of this material, however all features are not discernible in the photoemission intensity plots presented in Fig. 4(a). We present the dispersion maps along the high symmetry directions i.e. M-Γ-M, K-Γ-K, and K-M-K directions, respectively. Electron like bands are seen along the M-Γ-M and K-Γ-K directions. The presence of an electron like pocket at the Γ can be further confirmed by the constant energy contours presented in the SM [33]. Dispersion map along the M-Γ-M direction shows a quasi-two dimensional nature; as the band does not disperse with photon energies (26-120 eV) [33]. The 2D-like bands can be attributed to be originated from the orbitals related to the kagome lattice (Mn) [51]. Our orbital-projected first principles calculations show that electron-like bands along the Γ-K direction are contributed by Mn d_{xz} and Mn d_{z^2} (see Fig. S6 and Fig. S11 [33]). The dispersion maps along the K-M-K exhibit the lower Dirac cone-like features at the K points. The observation of Dirac cones at the K point, characteristics features observed in many other kagome materials, suggests the possible origin of the anomalous Hall effect in this material. Major ARPES features are captured in the first-principles calculations (see Fig. S11 for side by side comparison [33]), which suggest the presence of Dirac cone at the K point. Presence of various factors such as intrinsic magnetism, correlation, matrix elements effects, etc. play crucial roles for some discrepancies between ARPES and calculated plots.

A 3D system with quasi-2D electronic structures can provide a condition for the anomalous Hall effect originated from the Berry curvature. First-principles calculations predict that the Chern gap lies above the Fermi level. ARPES measurements and first-principles calculations indicate the orbital-selective Dirac fermiology as seen in various kagome materials [51–54]. As suggested by ref. [25], the controlling interaction in $ErMn_6Sn_6$ is mainly contributed by Mn-Mn interactions, therefore one can anticipate the crucial role of the kagome layer in this system for exotic magnetic and transport properties. Additionally, the flat bands cover almost all of the Brillouin zone, however they locate above the Fermi level. Thus, it does not contribute for the correlation. By possible electron-doping the flat band can be brought to Fermi level which could give rise to the correlated system. Further, replacing or doping with lighter compounds might add an interesting insight in these type of materials [55]. In conclusion, by performing detailed magneto-transport measurements, we report a direct observation of anisotropically large anomalous and topological Hall effect in $ErMn_6Sn_6$. Our combined experimental and theoretical investigations demonstrate the multi-orbital kagome band structure at the Fermi level. Our study suggests a new platform to study the interplay of correlation and magnetism in a kagome magnet system.

Acknowledgement

M.N. is supported by the Air Force Office of Scientific Research under award number FA9550-17-1-0415, the Air Force Office of Scientific Research MURI (FA9550-20-1-0322), and the Center for Thermal Energy Transport under Irradiation, an Energy Frontier Research Center funded by the U. S. DOE, Office of Basic Energy Sciences. F.C.K and P.M.O. acknowledge support from the Swedish Research Council (VR) and the Knut and Alice Wallenberg Foundation (Grant No. 2015.0060). Computational resources were provided by the Swedish National Infrastructure for Computing (SNIC)(Grant No. 2018-05973). Work at Buffalo State was supported by startup fund from SUNY Buffalo State College and the Office of Undergraduate Research Program. R.F. acknowledges financial support from Office of Undergraduate Research, EURO and Small Grant awards. N.P. and K.G. acknowledge support from the INL's LDRD program (18P37-008FP and 19P45-019FP, respectively) under DOE Idaho Operations Office Contract DE-AC07-05ID14517. We thank Donghui Lu, and Mokoto Hashimoto for beamline assistance.

* These authors contributed equally in this work.
† corresponding author: Madhab.Neupane@ucf.edu

[1] B. Keimer and J. Moore, Nat. Phys. **13**, 1045 (2017).
[2] S. Sachdev, Rep. Prog. Phys. **82**, 014001 (2018).
[3] K. He, Y. Wang, and Q.-K. Xue, Annu. Rev. Condens. Matter Phys. **9**, 329 (2018).
[4] M. M. Hosen, G. Dhakal, K. Dimitri, P. Maldonado, A. Aperis, F. Kabir, C. Sims, P. Riseborough, P. M. Oppeneer, D. Kaczorowski, et al., Sci. Rep. **8**, 13283 (2018).
[5] R. S. K. Mong, A. M. Essin, and J. E. Moore, Phys. Rev. B **81**, 245209 (2010).
[6] T.-H. Han, J. S. Helton, S. Chu, D. G. Nocera, J. A. Rodriguez-Rivera, C. Broholm, and Y. S. Lee, Nature **492**, 406 (2012).
[7] L. Ye, M. Kang, J. Liu, F. von Cube, C. R. Wicker, T. Suzuki, C. Jozwiak, A. Bostwick, E. Rotenberg, D. C. Bell, L. Fu, R. Comin, and J. G. Checkelsky, Nature **555**, 638 (2018).
[8] J.-X. Yin, S. S. Zhang, G. Chang, Q.Wang, S. S. Tsirkin, Z. Guguchia, B. Lian, H. Zhou, K. Jiang, I. Belopolski, et al., Nat. Phys. **15**, 443 (2019).
[9] J.-X. Yin, W. Ma, T. A. Cochran, X. Xu, S. S. Zhang, H.-J. Tien, N. Shumiya, G. Cheng, K. Jiang, B. Lian, Z. Song, G. Chang, I. Belopolski, D. Multer, M. Litskevich, Z.-J. Cheng, X. P. Yang, B. Swidler, H. Zhou, H. Lin, T.

Neupert, Z. Wang, N. Yao, T.-R. Chang, S. Jia, and M. Zahid Hasan, Nature **583**, 533 (2020).
[10] H. Chen, Q. Niu, and A. H. MacDonald, Phys. Rev. Lett. **112**, 017205 (2014).
[11] J.-X. Yin, S. S. Zhang, G. Chang, Q.Wang, S. S. Tsirkin, Z. Guguchia, B. Lian, H. Zhou, K. Jiang, I. Belopolski, 6 N. Shumiya, D. Multer, M. Litskevich, T. A. Cochran, H. Lin, Z. Wang, T. Neupert, S. Jia, H. Lei, and M. Z. Hasan, Nat. Phys. **15**, 443 (2019).
[12] E. Tang, J.-W. Mei, and X.-G. Wen, Phys. Rev. Lett. **106**, 236802 (2011).
[13] G. Xu, B. Lian, and S.-C. Zhang, Phys. Rev. Lett. **115**, 186802 (2015).
[14] I. I. Mazin, H. O. Jeschke, F. Lechermann, H. Lee, M. Fink, R. Thomale, and R. Valenti, Nat. Commun. **5**, 4261 (2014).
[15] S. Nakatsuji, N. Kiyohara, and T. Higo, Nature **527**, 212 (2015).
[16] K. Kuroda, T. Tomita, M. T. Suzuki, C. Bareille, A. A. Nugroho, P. Goswami, M. Ochi, M. Ikhlas, M. Nakayama, S. Akebi, R. Noguchi, R. Ishii, N. Inami, K. Ono, H. Kumigashira, A. Varykhalov, T. Muro, T. Koretsune, R. Arita, S. Shin, T. Kondo, and S. Nakatsuji, Nat. Mater. **16**, 1090 (2017).
[17] J.-X. Yin, S. S. Zhang, H. Li, K. Jiang, G. Chang, B. Zhang, B. Lian, C. Xiang, I. Belopolski, H. Zheng, T. A. Cochran, S.-Y. Xu, G. Bian, K. Liu, T.-R. Chang, H. Lin, Z.-Y. Lu, Z. Wang, S. Jia, W. Wang, and M. Z. Hasan, Nature **562**, 91 (2018).
[18] Z. Lin, J.-H. Choi, Q. Zhang, W. Qin, S. Yi, P. Wang, L. Li, Y. Wang, H. Zhang, Z. Sun, L. Wei, S. Zhang, T. Guo, Q. Lu, J.-H. Cho, C. Zeng, and Z. Zhang, Phys. Rev. Lett. **121**, 096401 (2018).
[19] E. Liu, Y. Sun, N. Kumar, L. Muechler, A. Sun, L. Jiao, S.-Y. Yang, D. Liu, A. Liang, Q. Xu, J. Kroder, V. Süß, H. Borrmann, C. Shekhar, Z. Wang, C. Xi, W. Wang, W. Schnelle, S. Wirth, Y. Chen, S. T. B. Goennenwein, and C. Felser, Nat. Phys. **14**, 1125 (2018).
[20] Q. Wang, S. Sun, X. Zhang, F. Pang, and H. Lei, Phys. Rev. B **94**, 075135 (2016).
[21] Q. Wang, Y. Xu, R. Lou, Z. Liu, M. Li, Y. Huang, D. Shen, H. Weng, S. Wang, and H. Lei, Nat. Commun. **9**, 3681 (2018).
[22] A. K. Nayak, J. E. Fischer, Y. Sun, B. Yan, J. Karel, A. C. Komarek, C. Shekhar, N. Kumar, W. Schnelle, J. Kübler, C. Felser, and S. S. P. Parkin, Sci. Adv. **2**, e1501870 (2016).
[23] W. Ma, X. Xu, Z. Wang, H. Zhou, M. Marshall, Z. Qu, W. Xie, and S. Jia, Phys. Rev. B **103**, 235109 (2021).
[24] W. Ma, X. Xu, J.-X. Yin, H. Yang, H. Zhou, Z.-J. Cheng, Y. Huang, Z. Qu, F.Wang, M. Z. Hasan, and S. Jia, Phys. Rev. Lett. **126**, 246602 (2021).
[25] D. Clatterbuck and K. Gschneidner Jr, J. Magn. Magn. Mater. **207**, 78 (1999).
[26] B. Malaman, G. Venturini, R. Welter, J. Sanchez, P. Vulliet, and E. Ressouche, J. Magn. Magn. Mater. **202**, 519 (1999).
[27] S. T. Yazdi, N. Tajabor, M. R. Roknabadi, M. Behdani, and F. Pourarian, J. Magn. Magn. Mater. **324**, 723 (2012).
[28] N. J. Ghimire, R. L. Dally, L. Poudel, D. C. Jones, D. Michel, N. T. Magar, M. Bleuel, M. A. McGuire, J. S. Jiang, J. F. Mitchell, J. W. Lynn, and I. I. Mazin, Sci. Adv. **6**, eabe2680 (2020).
[29] Q. Wang, K. J. Neubauer, C. Duan, Q. Yin, S. Fujitsu, H. Hosono, F. Ye, R. Zhang, S. Chi, K. Krycka, H. Lei, and P. Dai, Phys. Rev. B **103**, 014416 (2021).
[30] C. Mielke III, W. Ma, V. Pomjakushin, O. Zaharko, X. Liu, J.-X. Yin, S. Tsirkin, T. Cochran, M. Medarde, V. Poree, et al., arXiv:2101.05763 (2021).
[31] J.-l. Yao, S.-y. Zhang, B.-d. Liu, B.-g. Shen, R.-w. Wang, L.-g. Zhang, D.-r. Yang, and M. Yan, J. Appl. Phys. **95**, 7061 (2004).
[32] K. Suga, K. Kindo, L. Zhang, E. Brück, K. Buschow, F. De Boer, C. Lefèvre, and G. Venturini, Journal of alloys and compounds **408**, 158 (2006).
[33] See supplemental materials for details of methods, sample characterization, theoretical analysis, and ARPES data analysis.
[34] P. Hohenberg and W. Kohn, Phys. Rev. **136**, B864 (1964).
[35] W. Kohn and L. J. Sham, Phys. Rev. **140**, A1133 (1965).
[36] G. Kresse and J. Kübler, Phys. Rev. B **54**, 11169 (1996).
[37] G. Kresse and J. Kübler, Comput. Mater. Sci. **6**, 15 (1996).
[38] P. E. Bloochl, Phys. Rev. B **50**, 17953-17979 (1994).
[39] J. P. Perdew, K. Burke, M. Ernzerhof, Phys. Rev. Lett. **77**, 3865-3868 (1996).
[40] S. L. Dudarev, G. A. Botton, S. Y. Savrasov, C. J. Humphreys and A. P. Sutton, Phys. Rev. B **57**, 1505 (1998).
[41] H. J. Monkhorst, J. D. Pack, Phys. Rev. B **13**, 5188-5192 (1976).
[42] M. P. Lopez Sancho, J. M. Lopez Sancho, and J. Rubio, J. Phys. F: Met. Phys. **15**, 851 (1985).
[43] A. A. Mostofi, *et al.* Comput. Phys. Commun. **185**, 2309 (2014).
[44] Q. Wu, S. Zhang, H. Song, M. Troyer, and A. A. Soluyanov, Comput. Phys. Commun. **224**, 405 (2018).
[45] S. Onoda and N. Nagaosa, Phys. Rev. Lett. **90**, 196602 (2003).
[46] P. Bruno, V. K. Dugaev, and M. Taillefumier, Phys. Rev. Lett. **93**, 096806 (2004).
[47] Q. Wang, Q. Yin, S. Fujitsu, H. Hosono, and H. Lei, arXiv:1906.07986 (2019).
[48] L. Vistoli, W.Wang, A. Sander, Q. Zhu, B. Casals, R. Cichelero, A. Barthélémy, S. Fusil, G. Herranz, S. Valencia, R. Abrudan, E. Weschke, K. Nakazawa, H. Kohno, J. Santamaria, W. Wu, V. Garcia, and M. Bibes, Nat. Phys. **15**, 67 (2019).
[49] C. Sürgers, G. Fischer, P. Winkel, and H. v. Löhneysen, Nat. Commun. **5**, 3400 (2014).
[50] H. Li, B. Ding, J. Chen, Z. Li, E. Liu, X. Xi, G. Wu, and W. Wang, Appl. Phys. Lett. **116**, 182405 (2020).
[51] M. Li, Q. Wang, G. Wang, Z. Yuan, W. Song, R. Lou, Z. Liu, Y. Huang, Z. Liu, H. Lei, et al., Nat. commun. **12**, 3129 (2021).
[52] M. Kang, L. Ye, S. Fang, J.-S. You, A. Levitan, M. Han, J. I. Facio, C. Jozwiak, A. Bostwick, E. Rotenberg, M. K. Chan, R. D. McDonald, D. Graf, K. Kaznatcheev, E. Vescovo, D. C. Bell, E. Kaxiras, J. van den Brink, M. Richter, M. Prasad Ghimire, J. G. Checkelsky, and R. Comin, Nat. Mater. **19**, 163 (2020).
[53] Z. Liu, M. Li, Q. Wang, G. Wang, C. Wen, K. Jiang, X. Lu, S. Yan, Y. Huang, D. Shen, J.-X. Yin, Z. Wang, Z. Yin, H. Lei, and S. Wang, Nat. Commun. **11**, 4002 (2020).
[54] T. Yang, Q. Wan, Y. Wang, M. Song, J. Tang, Z. Wang,

H. Lv, N. Plumb, M. Radovic, G. Wang, et al., arXiv preprint arXiv:1906.07140 (2019).

[55] D. Chen, C. Le, C. Fu, H. Lin, W. Schnelle, Y. Sun, and C. Felser, Phys. Rev. B **103**, 144410 (2021).